Research Article Vol. 56, No. 31 / November 1 2017 / Applied Optics H51

applied optics

High-depth-resolution range imaging with multiple-wavelength superheterodyne interferometry using 1550-nm lasers

Fengqiang Li,[1,*] Joshua Yablon,[1] Andreas Velten,[2,3] Mohit Gupta,[4] and Oliver Cossairt[1]

[1]Department of Electrical Engineering and Computer Science, Northwestern University, 2145 Sheridan Road, Evanston, Illinois 60201, USA
[2]Department of Biostatistics and Medical Informatics, University of Wisconsin-Madison, 1300 University Ave, Madison, Wisconsin 53706, USA
[3]Department of Electrical and Computer Engineering, University of Wisconsin-Madison, 1300 University Ave, Madison, Wisconsin 53706, USA
[4]Department of Computer Science, University of Wisconsin-Madison, 1210 Dayton Street, Madison, Wisconsin 53706, USA
*Corresponding author: fengqiangli2015@u.northwestern.edu

Received 1 June 2017; revised 28 July 2017; accepted 22 August 2017; posted 23 August 2017 (Doc. ID 297083); published 15 September 2017

Lasers and laser diodes are widely used as illumination sources for optical imaging techniques. Time-of-flight (ToF) cameras with laser diodes and range imaging based on optical interferometry systems using lasers are among these techniques, with various applications in fields such as metrology and machine vision. ToF cameras can have imaging ranges of several meters, but offer only centimeter-level depth resolution. On the other hand, range imaging based on optical interferometry has depth resolution on the micrometer and even nanometer scale, but offers very limited (sub-millimeter) imaging ranges. In this paper, we propose a range imaging system based on multi-wavelength superheterodyne interferometry to simultaneously provide sub-millimeter depth resolution and an imaging range of tens to hundreds of millimeters. The proposed setup uses two tunable III-V semiconductor lasers and offers leverage between imaging range and resolution. The system is composed entirely of fiber connections except the scanning head, which enables it to be made into a portable device. We believe our proposed system has the potential to tremendously benefit many fields, such as metrology and computer vision. © 2017 Optical Society of America

OCIS codes: (140.0140) Lasers and laser optics; (100.3175) Interferometric imaging; (110.0110) Imaging systems.

https://doi.org/10.1364/AO.56.000H51

1. INTRODUCTION

Range or three-dimensional (3D) imaging techniques using lasers or laser diodes as illumination sources can provide depth information of objects being scanned. These optical range imaging techniques have lots of important applications, such as metrology [1] and machine vision, especially for robots and self-driving cars [2,3]. Among these range-imaging techniques, time-of-flight (ToF) cameras with a laser diode as the illumination source and range imaging based on interferometry are two important types of systems. For range-imaging techniques, higher depth resolution and longer imaging range are always sought, in order to resolve finer details of an object and image larger-scale objects.

Recently, ToF cameras have been a promising range-imaging technique due to cost efficiency and compact size [4–7] compared with light detection and ranging (lidar) devices [8]. ToF cameras have been widely used in machine perception and tracking applications such as Microsoft's Kinect [9] and machine vision for robots [10]. ToF cameras typically employ high-frequency (generally 10–100 MHz) amplitude modulation of the laser output. The modulating signal is simultaneously sent to ToF camera pixels as a reference. Correlation and demodulation between the reference signal and the reflection signal from the object are obtained to calculate depth information. ToF cameras can provide an unambiguous imaging range of several meters and depth resolution on the centimeter level [11]. The expression governing the correlation I_t between the reference and the received light is presented in Eq. (1) [12], which shows that the modulation frequency f_t controls the depth resolution. In order to increase depth resolution, higher modulation frequency is needed. However, depth resolution on the micrometer level is not possible because ToF sensors cannot be modulated at GHz frequencies.

On the other hand, range imaging based on laser interferometry has depth resolution on the micrometer or nanometer scale and is used widely in metrology and biophotonics imaging to resolve fine features of various structures [13–19]. In optical-interferometry-based range imaging, a continuous wave laser is split into two beams with one beam illuminating the object and the other beam used as a reference. The optical frequency (f_o)

serves as the modulation frequency. The detector receives the interference signal I_o [as shown in Eq. (1)] between the reflection beam from the object and the reference beam [14]. Since the modulation frequency f_o is on the order of 10^{14} Hz, the depth resolution is much higher than that of ToF cameras. The drawback to this high depth resolution is sub-millimeter imaging range. Furthermore, this system can operate only on critical platforms, such as isolated optical tables. In order to solve the problem of limited imaging range, the optical frequency can be decreased by orders of magnitude to generate millimeter or centimeter imaging range. However, stable sources of coherent electromagnetic radiation with such long wavelengths do not exist

$$I_i = \alpha_i + \beta_i \cos\left(4\pi \frac{f_i}{c} z + \phi_i\right); \qquad i = t, o, p. \tag{1}$$

Equation (1) (t: ToF cameras; o: range imaging based on optical interferometry; p: proposed solution) shows the outputs in ToF cameras and interferometry-based range imaging with z representing the distance from the sensor to the point of interest on the object, while c is the speed of light. α_i, β_i, and ϕ_i are constants with different values in different imaging models. This equation shows that the modulation frequency controls both depth resolution and imaging range and that there is a tradeoff between these two parameters. [In Eq. (1), the depth information can be demodulated with a phase of $4\pi(f_i/c)z$. The maximum achievable phase difference without phase wrapping is 2π. Imaging range can be calculated with this maximum phase value. Therefore, the higher the modulation frequency, the shorter the imaging range. For depth resolution, we assume that the resolution is limited by the sensor SNR. The phase $4\pi(f_i/c)z$ ranges from 0 to 2π and is demodulated by using the intensity information I_i. Suppose the number of gray levels in the detectors is N. Then each gray level represents the resolution of the imaging system as $c/(2Nf_i)$. Therefore, the higher the frequency, the higher the depth resolution.] The motivation of this study is therefore to generate a GHz or even THz frequency f_p with the same output model as shown in Eq. (1) in order to have micrometer depth resolution, while simultaneously having an imaging range of several hundred millimeters.

In this paper, we propose an imaging system using superheterodyne interferometry [20] where two 1550-nm III–V semiconductor lasers with slightly different optical frequencies are used to generate a GHz-frequency optical beat-note signal used for detection. In the following sections, a mathematical model is developed and simulations are performed based on this proposed method, and a prototype system is built and tested. This setup allows flexibility between imaging range and depth resolution, since the lasers are tunable. Furthermore, the system can be operated in noisy environments and is completely fiber based, which makes the device portable.

2. EXPERIMENTAL SETUP

The schematic of our proposed setup is shown in Fig. 1. The system is constructed with two InP tunable lasers (PPCL200, Pure Photonics) with a center wavelength of ~1550 nm. The linewidth of each tunable laser is ~10 KHz, which corresponds

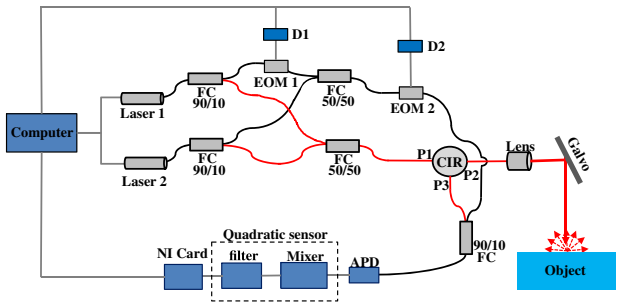

Fig. 1. Schematic of our proposed setup: Two tunable lasers are used as the illumination sources. FC, fiber coupler; EOM, eletro-optic modulator; CIR, fiber circulator; APD, avalanche photo-diode; D1, driver for EOM 1; and D2, driver for EOM 2. All fibers are polarization maintaining. The NI card and the two drivers are controlled with a computer. Red lines, sample arm. Black lines, reference arm.

to a coherence length of several tens of kilometers. Fiber couplers (FCs) are used to split and combine the beams, while electro-optic modulators (EOMs) are used to modulate the phase of the light. The galvo scans the beam across different points on the object, and an avalanche photodiode (APD) detects the interference signal.

The beams from the two lasers are split by 90/10 fiber couplers with 90% of the input beams directed toward the sample arm. The two beams in the reference arm are combined, with half of each input beam directed toward the circulator. The combined beam is then guided to port P1 of the fiber circulator, which directs the beam to the collimator and galvo scanner. The beam reflected from the object is collimated with a lens and directed from port P2 to port P3 to the detector. In the reference arm, the beam from laser 1 first goes though EOM 1 (LN53S-FC, Thorlabs), which sweeps the phase of the beam with values of $-\pi/2$, 0, $\pi/2$ to π. The beam after EOM 1 is then combined with the beam from laser 2, with half of each beam guided to EOM 2 (the same model as EOM 1), which introduces a high-frequency sinusoidal phase modulation to the beam. The beam from the reference arm is combined with the beam from the circulator port P3 by a 90/10 fiber coupler with 90% of the sample arm beam directed toward the APD. The interference signal between these two beams is detected by the APD (APD430C, Thorlabs). The APD converts the optical signal into an electrical signal, which is then sent into a quadratic sensor. This quadratic sensor contains a frequency mixer and a low-pass filter with cutoff frequency of 1.9 MHz. An NI data acquisition (DAQ) card (PCIe 6363, National Instruments) digitizes the signal. The depth information for one point on the object can then be calculated by using the four phase measurements. This process is then repeated for each point along the scan.

3. MATHEMATICAL MODEL

The mathematical model governing this proposed system is described in this section. The effect of environmental vibration to the system is modeled using a velocity-based vibration model [21]. The intensities of lasers 1 and 2 are constants with values of $\|E_1\|^2$ and $\|E_2\|^2$, respectively. The wavelengths of lasers 1 and 2 are λ_1 and λ_2, respectively. The electric field of the beam

reflected from the object to the detector is $E_s(t)$, and the electric field of the reference beam going into the detector is $E_r(t)$, and can be written as

$$E_s(t) = \alpha_1\beta E_1 e^{i\left(2\pi\nu_1 t+\frac{Vt}{\lambda_1}+\frac{4\pi}{\lambda_1}L_s\right)} + \alpha_2\beta E_2 e^{i\left(2\pi\nu_2 t+\frac{Vt}{\lambda_2}+\frac{4\pi}{\lambda_2}L_s\right)}, \quad (2)$$

$$E_r(t) = \gamma_1 E_1 e^{i\left(2\pi\nu_1 t+\frac{4\pi}{\lambda_1}L_r+\psi+2\pi ft\right)} + \gamma_2 E_2 e^{i\left(2\pi\nu_2 t+\frac{4\pi}{\lambda_2}L_r+2\pi ft\right)}, \quad (3)$$

where α_1, α_2, γ_1, and γ_2 are intensity reduction factors due to beam splitting and fiber insertion loss. β is the efficiency of beam reflection from the object surface. ν_1 and ν_2 are the optical frequencies of laser 1 and laser 2, respectively. V represents the velocity value in the velocity-based vibration model as described above. L_r is the optical path length for the light traveling in the reference arm, while L_s is the optical path length for the sample arm, which encodes the depth information of the object. ψ is the phase added by EOM 1, and f is the modulation frequency of EOM 2.

The beam reflected from the object surface interferes with the reference beam when they meet in the fiber coupler. The optical signal $I(t)$ going into the APD can be written as follows (the APD converts the photonic signal into an electrical signal):

$$\begin{aligned} I(t) &= (E_s(t) + E_r(t)) \times (E_s(t)^* + E_r(t)^*) \\ &= a_0 + a_1 \cos\left(\frac{Vt}{\lambda_1} + \phi_1 - \psi - 2\pi ft\right) \\ &\quad + a_2 \cos\left(\frac{Vt}{\lambda_2} + \phi_2 - 2\pi ft\right), \end{aligned} \quad (4)$$

where $a_0 = (\alpha_1\beta E_1)^2 + (\gamma_1 E_1)^2 + (\alpha_2\beta E_2)^2 + (\gamma_2 E_2)^2$, $a_1 = 2\alpha_1\beta\gamma_1 E_1^2$, and $a_2 = 2\alpha_2\beta\gamma_2 E_2^2$. a_0, a_1, and a_2 are constants. $\phi_1 = 4\pi L/\lambda_1$, and $\phi_2 = 4\pi L/\lambda_2$. L is equal to $(L_s - L_r)$, which is the optical path length difference between the sample and reference arms.

In order to generate a GHz beat-note frequency $(\nu_1 - \nu_2)$, the electrical signal from the APD is sent into a "quadratic sensor," which is a frequency mixer combined with a low-pass filter. The signal after the mixer, $S(t)$, is as follows:

$$\begin{aligned} S(t) = I(t)^2 = \Bigg[a_0 + a_1 \cos\left(\frac{Vt}{\lambda_1} + \phi_1 - \psi - 2\pi ft\right) \\ + a_2 \cos\left(\frac{Vt}{\lambda_2} + \phi_2 - 2\pi ft\right)\Bigg]^2. \end{aligned} \quad (5)$$

$S(t)$ contains DC components, components with frequency of f, and $2f$-frequency components. The low-pass filter removes the f and $2f$ components, so that the signal after the low-pass filter $L(t)$ is

$$L(t) = m_1 \cdot \cos\left(\frac{Vt}{\Lambda} + \frac{4\pi L}{\Lambda} - \psi\right) + m_2, \quad (6)$$

where $m_1 = a_1 a_2$, and m_2 is a constant. Λ is the so-called "synthetic wavelength," which is equal to $\lambda_1\lambda_2/(\lambda_2 - \lambda_1)$.

A DAQ card converts the analog signal $(L(t))$ into a digital signal $(o(t))$ with satisfying Nyquist sampling condition. The synthetic wavelength is determined by the selection of λ_1 and λ_2 and is on the order of tens of millimeters in our experiment. The synthetic wavelength is much larger than the amplitude of most mechanical vibrations, thus rendering vibration effects negligible. The output signal is then

$$\begin{aligned} o(t) &= m_1 \cos\left(\frac{Vt}{\Lambda} + \frac{4\pi L}{\Lambda} - \psi\right) + m_2 \\ &\approx m_1 \cos\left(\frac{4\pi L}{\Lambda} - \psi\right) + m_2. \end{aligned} \quad (7)$$

Since Λ equals $c/(\nu_1 - \nu_2)$, the output signal $o(t)$ can be written as

$$o(t) = m_1 \cos\left(4\pi\frac{\Delta\nu}{c}L - \psi\right) + m_2, \quad (8)$$

where $\Delta\nu$ equals $(\nu_1 - \nu_2)$. Therefore, a new frequency $\Delta\nu$ with a value tunable anywhere from DC to THz range is generated, as proposed in Eq. (1).

Four measurements are taken at phase values of $-\pi/2$, 0, $\pi/2$, π using EOM 1 [4]:

$$o_1 = o_a \cos\left(4\pi\frac{\Delta\nu}{c}L\right) + o_b, \quad (9)$$

$$o_2 = o_a \cos\left(4\pi\frac{\Delta\nu}{c}L - \frac{\pi}{2}\right) = o_a \sin\left(4\pi\frac{\Delta\nu}{c}L\right) + o_b, \quad (10)$$

$$o_3 = o_a \cos\left(4\pi\frac{\Delta\nu}{c}L - \pi\right) = -o_a \cos\left(4\pi\frac{\Delta\nu}{c}L\right) + o_b, \quad (11)$$

$$o_4 = o_a \cos\left(4\pi\frac{\Delta\nu}{c}L - \frac{3\pi}{2}\right) = -o_a \sin\left(4\pi\frac{\Delta\nu}{c}L\right) + o_b. \quad (12)$$

The depth information (L) can be calculated as

$$L = \frac{c}{4\pi\Delta\nu} \arctan\left(\frac{o_2 - o_4}{o_1 - o_3}\right). \quad (13)$$

This process can be repeated for all points on the object's surface using a galvo scanner.

4. SIMULATION

To theoretically validate the concept of this proposed imaging system, we performed a simulation based on the mathematical model. The wavelengths of the two lasers are set as 1550 nm and 1550.01 nm. The velocity of the environmental vibration is set at 1 mm/s. The intensity reductions of α_1 and α_2 are set at 0.49 for the sample arm, and γ_1 and γ_2 are set at 0.001. The modulation frequency of EOM 2 is 15 MHz. The object is modeled with the Lambertian model. White noise with SNR of 27.8 dB is added to the APD readout. Another white noise source with SNR of 29 dB is added in the analog-to-digital (ADC) conversion.

The signal processing flow for a single point on the surface of the object is shown in Fig. 2. The APD output of the received interference signal is shown in Fig. 2(a). As shown in Fig. 2(b) of the interference sginal's spectrum, the 15-MHz frequency component is resolved by the APD. The mixer output is shown in Fig. 2(c) with its spectrum shown in Fig. 2(d). The DC component, 15-MHz component, and 30-MHz

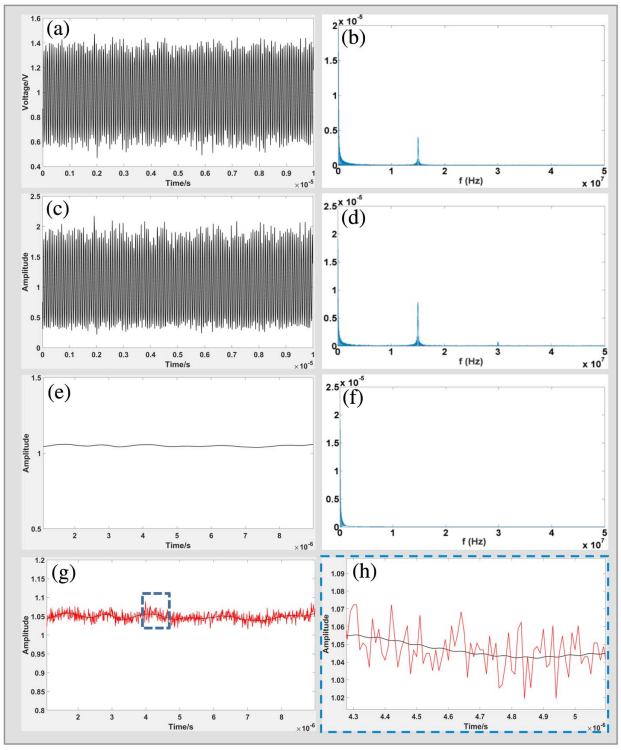

Fig. 2. Signal processing flow for one point: (a) simulated APD output; (b) spectrum of simulated APD output; (c) signal after the mixer in the quadratic sensor; (d) spectrum of mixer output; (e) signal after the quadratic sensor; (f) spectrum of the quadratic sensor output; (g) analog-to-digital conversion by the DAQ card (red line) of the quadratic sensor output (black line); and (h) inset of the signal in (g).

component are clearly observed. The 15- and 30-MHz components are removed by the low-pass filter, as shown in Fig. 2(e) with its spectrum shown in Fig. 2(f). White noise is added to the low-pass filter output and then sampled with

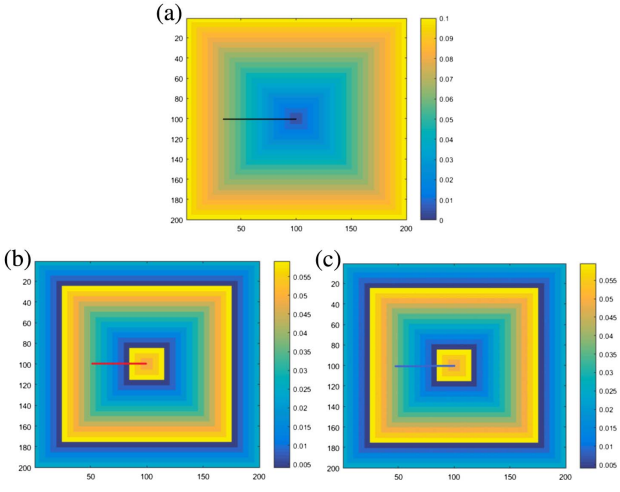

Fig. 3. (a) Groundtruth 3D objects; (b) simulated 3D images with no noise added in the APD and the NI card; and (c) simulated 3D images with noise added. The x axis and the y axis mark the pixel number in the x and y dimensions. Different colors represent the depth information with values from 0 to 100 mm. Color bar units are in meters.

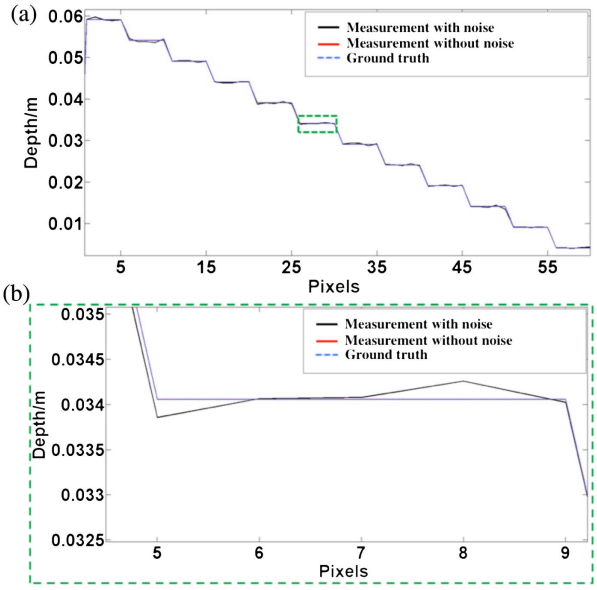

Fig. 4. A line plot across the simulated 3D object in Fig. 3(a), depth values on pixels along the line in simulated measurement with noise, simulated measurement without noise, and ground truth. The imaging range is about 60 mm as shown in the plot; (b) inset of (a) shows a zoomed-in offset between measurements and the ground truth. There is overlap between the noiseless simulated measurement and the ground truth.

the DAQ card, as shown in Figs. 2(g) and 2(h) (marked with red line). The depth information is calculated with the previous four-bucket method by sweeping the phase in EOM 1.

A 3D object containing many stair-steps with depth ranging from 0 to 100 mm with a step of 5 mm (from center to edge) is generated as the ground truth shown in Fig. 3(a). The depth information for the whole object calculated using the previous method without noise is shown in Fig. 3(b), while the depth information with noise is shown in Fig. 3(c). Phase wrapping occurs if the depth is larger than the imaging range of 60 mm, as shown in Figs. 3(b) and 3(c). The cross-lines at the same location in Figs. 3(a)–3(c) are shown in Fig. 4. The simulated measurement with noise is compared to the no-noise data and the ground truth data, as shown in the inset [Fig. 4(b)]. The difference ΔL between simulated measurements with noise and ground truth was compared and analyzed. The mean of ΔL is 0.0026 mm with a standard deviation of 0.2226 mm. This indicates that the depth resolution is far less than 1 mm, with an imaging range of 60 mm. This gives the credibility to the concept of our proposed imaging system.

5. EXPERIMENTS AND RESULTS

After validating this system, we built an experimental prototype as previously described. The wavelengths of the two tunable lasers are 1550 nm and 1550.04 nm. The offset between λ_1 and λ_2 in the prototype is set to be larger than that in the simulation experiment to make the optical beat-note frequency stable. The output power of each laser is about 25 mW. A custom-made driver controlled by the DAQ card is used to drive EOM 1. Another driver is used to drive EOM 2 with

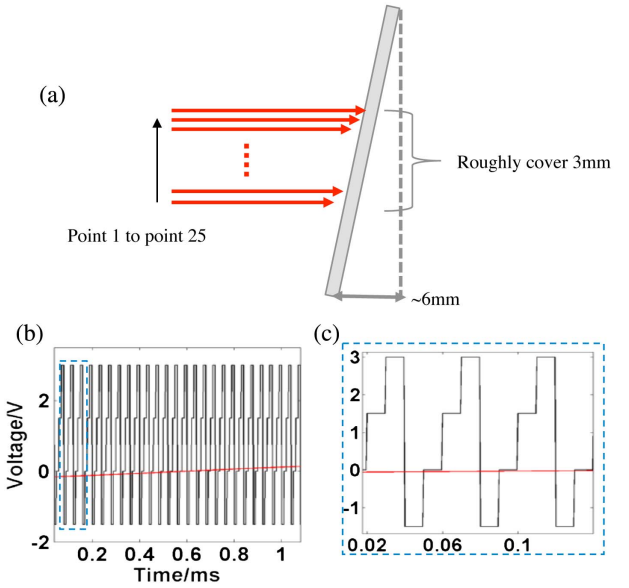

Fig. 5. (a) Tilted plane being measured along with the schematic of the scan; (b) driving signals to EOM 1 and galvo scanner; and (c) inset of (b).

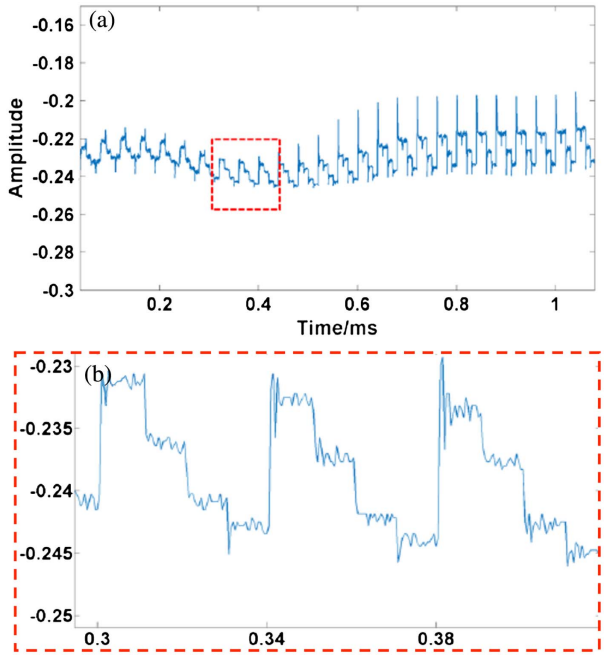

Fig. 6. (a) DAQ card readout shows the phase-modulated signal; and (b) inset of (a).

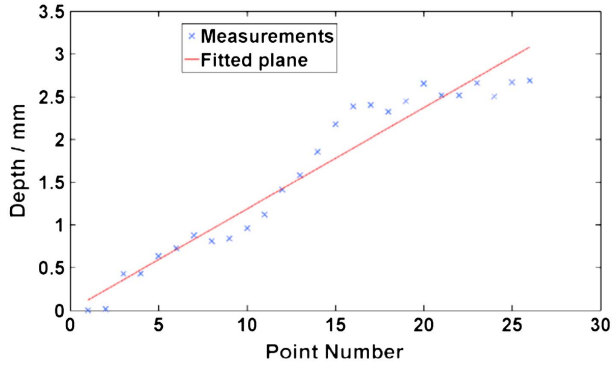

Fig. 7. Results and the depth calculated. (a) Phase value calculated at different points; and (b) corresponding depth information.

a modulation frequency of 15 MHz. A low-pass filter with a cutoff frequency of 22 MHz is used to remove high-harmonic components of the output from driver 2 before sending this driver output to EOM 2. The half-wave voltage of EOM 1 is approximately 3 volts.

The interference signal at the APD was found to be unstable on the tens-of-ms to several-seconds timescale (see more details below). Therefore, it was necessary to make measurements on the sub-ms timescale to demonstrate the high depth resolution of the proposed system. The depth information of a tilted planar surface was measured. The tilt level (the distance between the nearest point and farthest point) of the plane was ~6 mm. The galvo scanned 25 points in 1 ms, as shown in Fig. 5(a). The galvo was scanned using a sinusoidal signal with frequency of 500 Hz, as marked with the red line in Fig. 5(b). The driving signal to EOM 1 is the black step signal shown in Figs. 5(b) and 5(c). The DAQ card readout of the superheterodyne signal, as shown in Fig. 6, shifts when the phase is swept on EOM 1 by adding different voltages. There appears to be good correspondence between the DAQ card readout (Fig. 6) and the modulation signal [Fig. 5(c)].

The corresponding depth information for these 25 consecutively scanned points was calculated based on the four-bucket method, with the results shown in Fig. 7. A best-fit line was fitted for the measurements, as indicated by the red line in Fig. 7. We quantified the difference between the measurements and the best-fit line for all points. The mean deviation between the measured depth and best-fit depth is 0.1824 mm with a standard deviation of 0.1391 mm. This preliminary result proves the possibility of our proposed setup for sub-millimeter depth resolution.

Although this prototype demonstrates good depth resolution, the imaging range is limited due to noise in the system. The main sources of noise are the hardware components, such as EOMs and lasers. The output fibers of EOMs are not polarization-maintaining (PM) fibers. Thus, small environmental perturbations (e.g., vibrations, air currents, temperature fluctuations) can create polarization rotation in the EOM output, which then causes the interference pattern to fluctuate randomly. In the next iteration of our prototype, every component in the device will be PM, so that this issue will cease to exist. Another noise source is that each laser fluctuates in frequency over a range of approximately 20 MHz on the seconds timescale. These frequency fluctuations increase the uncertainty in the synthetic wavelength, which decreases both the depth resolution and the imaging range. In principle, there are many methods to fix or circumvent this problem [22–26]. The most promising method is offset phase locking, in which one laser is locked to the other so that the difference frequency remains constant [27]. This random drift can also be circumvented

to some extent by using a synthetic wavelength that corresponds to a very high beat-note frequency, so that the 40-MHz beat-frequency drift is less significant. For example, if the synthetic frequency is set to 4 GHz, then a 40-MHz uncertainty would correspond to an uncertainty in the beat-note (and therefore an uncertainty in the synthetic wavelength) of one percent. Finally, another way to circumvent this issue would be to create a second "reference arm" that would be used to measure and subtract the random drift when performing depth calculations.

The next step is to design and build a new experimental system that can solve the hardware instability issues. Offset phase locking the lasers and replacing EOMs with acousto-optic modulators (AOMs) should make the system work for the entire proposed frequency range, and should make it more reliable. We believe this new system will fill an important niche between 3D imaging based on optical interferometry and ToF imaging.

6. CONCLUSION

In conclusion, we have proposed a fiber-based multi-wavelength interferometry system using two 1550-nm lasers to achieve sub-millimeter depth resolution and an imaging range of several tens of centimeters. Our simulation and preliminary experimental results have demonstrated that this idea is promising. This system is more robust than other standard imaging systems because it has a long imaging range, high resolution, is portable, and does not need to be operated in an isolated environment. This system can benefit the field of metrology by providing high-accuracy depth measurement with long image range simultaneously. It also has the potential to provide high-accuracy 3D models applicable to the fields of computer vision and computer graphics applications, such as 3D human face scanning.

Funding. National Science Foundation (NSF) (IIS-1453192); Office of Naval Research (ONR) (N00014-15-1-2735); Defense Advanced Research Projects Agency (DARPA) (HR0011-16-C-0028).

Acknowledgment. The authors would like to thank Shih Tseng for building a custom driver for EOM 1.

REFERENCES

1. K. J. Gåsvik, *Optical Metrology* (Wiley, 2003).
2. S. Se and P. Jasiobedzki, "Photo-realistic 3D model reconstruction," in *Proceedings of IEEE International Conference on Robotics and Automation* (2006), pp. 3076–3082.
3. J. Levinson, J. Askeland, J. Becker, J. Dolson, D. Held, S. Kammel, J. Z. Kolter, D. Langer, O. Pink, V. Pratt, M. Sokolsky, G. Stanek, D. Stavens, A. Teichman, M. Werling, and S. Thrun, "Towards fully autonomous driving: systems and algorithms," in *IEEE Intelligent Vehicles Symposium* (2011), pp. 163–168.
4. R. Lange and P. Seitz, "Solid-state time-of-flight range camera," IEEE J. Quantum Electron. **37**, 390–397 (2001).
5. T. Möller, H. Kraft, J. Frey, M. Albrecht, and R. Lange, "Robust 3D measurement with PMD sensors," Range Imaging Day, Zürich **7**, 8 (2005).
6. R. Lange, P. Seitz, A. Biber, and S. C. Lauxtermann, "Demodulation pixels in CCD and CMOS technologies for time-of-flight ranging," in *Electronic Imaging* (International Society for Optics and Photonics, 2000), pp. 177–188.
7. R. Schwarte, Z. Xu, H.-G. Heinol, J. Olk, R. Klein, B. Buxbaum, H. Fischer, and J. Schulte, "New electro-optical mixing and correlating sensor: facilities and applications of the photonic mixer device (PMD)," in *Lasers and Optics in Manufacturing III* (International Society for Optics and Photonics, 1997), pp. 245–253.
8. C. Weitkamp, *Lidar: Range-Resolved Optical Remote Sensing of the Atmosphere* (Springer, 2006), Vol. **102**.
9. Z. Zhang, "Microsoft Kinect sensor and its effect," IEEE MultiMedia **19**, 4–10 (2012).
10. J. Sturm, N. Engelhard, F. Endres, W. Burgard, and D. Cremers, "A benchmark for the evaluation of RGB-D SLAM systems," in *IEEE/RSJ International Conference on Intelligent Robots and Systems (IROS)* (IEEE, 2012), pp. 573–580.
11. S. Foix, G. Alenya, and C. Torras, "Lock-in time-of-flight (TOF) cameras: a survey," IEEE Sens. J. **11**, 1917–1926 (2011).
12. F. Heide, M. B. Hullin, J. Gregson, and W. Heidrich, "Low-budget transient imaging using photonic mixer devices," ACM Trans. Graph. (ToG) **32**, 45 (2013).
13. J. H. Bruning, D. R. Herriott, J. E. Gallagher, D. P. Rosenfeld, A. D. White, and D. J. Brangaccio, "Digital wavefront measuring interferometer for testing optical surfaces and lenses," Appl. Opt. **13**, 2693–2703 (1974).
14. T. Dresel, G. Häusler, and H. Venzke, "Three-dimensional sensing of rough surfaces by coherence radar," Appl. Opt. **31**, 919–925 (1992).
15. H. Haitjema, "Achieving traceability and sub-nanometer uncertainty using interferometric techniques," Meas. Sci. Technol. **19**, 084002 (2008).
16. Z. Wang, B. Potsaid, L. Chen, C. Doerr, H.-C. Lee, T. Nielson, V. Jayaraman, A. E. Cable, E. Swanson, and J. G. Fujimoto, "Cubic meter volume optical coherence tomography," Optica **3**, 1496–1503 (2016).
17. D. Huang, E. A. Swanson, C. P. Lin, J. S. Schuman, W. G. Stinson, W. Chang, M. R. Hee, T. Flotte, K. Gregory, C. A. Puliafito, and J. G. Fujimoto, "Optical coherence tomography," Science **254**, 1178–1181 (1991).
18. F. Li, Y. Song, A. Dryer, W. Cogguillo, Y. Berdichevsky, and C. Zhou, "Nondestructive evaluation of progressive neuronal changes in organotypic rat hippocampal slice cultures using ultrahigh-resolution optical coherence microscopy," Neurophotonics **1**, 025002 (2014).
19. F. Li, T. Xu, D.-H. T. Nguyen, X. Huang, C. S. Chen, and C. Zhou, "Label-free evaluation of angiogenic sprouting in microengineered devices using ultrahigh-resolution optical coherence microscopy," J. Biomed. Opt. **19**, 016006 (2014).
20. R. Dändliker, R. Thalmann, and D. Prongué, "Two-wavelength laser interferometry using superheterodyne detection," Opt. Lett. **13**, 339–341 (1988).
21. C. G. Gordon, "Generic vibration criteria for vibration-sensitive equipment," Proc. SPIE **3786**, 22–33 (1999).
22. M. Reich, R. Schieder, H. J. Clar, and G. Winnewisser, "Internally coupled Fabry-Perot interferometer for high precision wavelength control of tunable diode lasers," Appl. Opt. **25**, 130–135 (1986).
23. L. Goldberg, H. Taylor, and J. Weller, "Fm sideband injection locking of diode lasers," Electron. Lett. **18**, 1019–1020 (1982).
24. M. De Labachelerie, K. Nakagawa, Y. Awaji, and M. Ohtsu, "High-frequency-stability laser at 1.5 μm using doppler-free molecular lines," Opt. Lett. **20**, 572–574 (1995).
25. Y. Chung and C. Roxlo, "Frequency-locking of a 1.5 μm DFB laser to an atomic krypton line using optogalvanic effect," Electron. Lett. **24**, 1048–1049 (1988).
26. R. J. Jones and J.-C. Diels, "Stabilization of femtosecond lasers for optical frequency metrology and direct optical to radio frequency synthesis," Phys. Rev. Lett. **86**, 3288–3291 (2001).
27. F. Friederich, G. Schuricht, A. Deninger, F. Lison, G. Spickermann, P. H. Bolívar, and H. G. Roskos, "Phase-locking of the beat signal of two distributed-feedback diode lasers to oscillators working in the MHz to THz range," Opt. Express **18**, 8621–8629 (2010).